Food Hydrocolloids 165 (2025) 111247

Contents lists available at ScienceDirect

Food Hydrocolloids

journal homepage: www.elsevier.com/locate/foodhyd

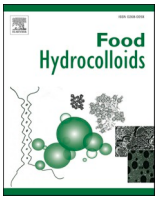

Air-water interfacial and foaming properties of lupin protein-polysaccharide soluble complexes: Role of physicochemical properties, morphological characteristics, and flexibility

Xingfa Ma *, Mehdi Habibi, Leonard M.C. Sagis

Laboratory of Physics and Physical Chemistry of Foods, Wageningen University, Bornse Weilanden 9, 6708 WG, Wageningen, the Netherlands

ARTICLE INFO

Keywords:
Lupin protein
κ-carrageenan
Pectin
Sodium alginate
Morphological properties
Interfacial structure and rheology
Foaming properties

ABSTRACT

Lupin protein isolate (LPI) has poor foaming properties in acidic conditions. The addition of polysaccharides to form electrostatic complexes with LPI at acidic pH was used to improve the foaming properties of LPI. This study mainly investigated the role of morphological properties and flexibility of LPI-polysaccharide complexes in stabilizing air-water interfaces and foams. Three polysaccharides were chosen with different chain flexibility, namely κ-carrageenan (KC), pectin (PC), and sodium alginate (SA), to make electrostatic complexes with LPI at a 1:1 ratio and pH 4.0. Dynamic light scattering (DLS) and atomic force microscopy were used to study particle size and morphology of the complexes. LPI-KC formed a large complex (~488.7 nm), consisting of several κ-carrageenan chains and large globular protein clusters, and formed a highly cross-linked structure, most likely linked by protein molecules and small protein clusters. LPI-PC formed a "core-shell-like" complex (~267.2 nm), where the complexes appear to have a dense core with pectin chains protruding from that core. LPI-SA formed a smaller more linear complex (~197.6 nm) that most likely consisted of bundles of polysaccharide chains held together by several protein molecules through attractive electrostatic interactions. Automatic droplet tensiometer (ADT) and AFM coupled with Langmuir-Blodgett deposition were used to study the interfacial properties of the complexes. LPI-PC and LPI-SA adsorbed faster to the air-water interface but formed interfaces with lower stiffness in the early adsorption phase than LPI-KC. After 3 h adsorption, LPI-KC formed a strong 2d gel-like air-water interface with the highest interfacial stiffness, while LPI-SA formed a soft glassy-like interface with a weaker interfacial stiffness than LPI-KC and LPI-PC. As a result, the LPI-KC stabilized foams showed the highest stability, followed by the LPI-PC stabilized foams, while the LPI-SA stabilized foams showed the lowest stability. Findings from this study revealed the relationship between the conformation of complexes and the air-water interfacial and foaming properties, which could be used to tailor the molecular properties of protein-polysaccharide complexes to achieve their optimal functionality in aerated food products.

1. Introduction

Traditionally, lupins were predominantly used as animal feed (White & Staines, 2007) and only to a limited extent for human consumption due to the presence of alkaloids (Rodés-Bachs & Van der Fels-Klerx, 2023). Nowadays, lupins (e.g., Lupinus spp.) have gained increasing interest as food ingredients due to their high nutritional benefits (Boukid & Pasqualone, 2022). Lupins mainly consist of proteins (~40%), dietary fiber (~28%), minerals, and a small amount of fat (~6%) (Guemes-Vera et al., 2012). Currently, lupin proteins are isolated mainly using three methods: (1) alkaline extraction followed by isoelectric precipitation or ultrafiltration; (2) micellization (salt extraction followed by dilutive precipitation); and (3) acid extraction (Shrestha, van't Hag, Haritos, & Dhital, 2021). Lupin proteins can be potentially used in the food industry, due to their good functional properties such as foaming, emulsifying, and gelling properties (Alamanou & Doxastakis, 1997; Muranyi et al., 2016). The major types of proteins in lupin seeds were classified into four categories, namely α-, β-, γ-, and δ-conglutin (Lo et al., 2020), of which α- and β-conglutin account for around 35–37% and 44–45% of the total protein, while γ- and δ-conglutin only account for around 4–5% and 10–12% of the total protein (Melo et al., 1994). Lupin proteins also showed promising techno-functional properties, which can be

* Corresponding author.
E-mail address: xingfa.ma@wur.nl (X. Ma).

https://doi.org/10.1016/j.foodhyd.2025.111247
Received 5 September 2024; Received in revised form 11 February 2025; Accepted 17 February 2025
Available online 18 February 2025

potentially used in the food industry (Ceresino et al., 2021; Lo et al., 2020).

Polysaccharides are widely used in the food industry (Aspinall, 2014). K-carrageenan, a sulfated polysaccharide of galactose, is widely used in the food industry as a gelling agent (Tanoeiro et al., 2023). Pectin, a galacturonic acid-based polysaccharide, is essential in jam and jelly production due to its strong gelling properties (Mohnen, 2008). Sodium alginate, a linear polysaccharide composed of a backbone of (1–4) linked β-d-mannuronic acid (M units) and α-l-guluronic acid (G units), is widely used in food, pharmaceutical, and biotechnology applications as a thickening and gelling agent (Ahmad et al., 2023).

In a previous study (Ma et al., 2024a), lupin protein at pH 4.0 showed better air-water interfacial and foaming properties than at other pH values. However, the poor solubility of lupin protein at pH 4.0 (~56%) limits its application in acidic food beverages. Using only the soluble fractions is not sustainable, while the retention of insoluble particles can be detrimental to the foaming properties. It is therefore important to improve the protein solubility or dispersibility at acidic pH. An often-adapted method to improve protein solubility is through electrostatic complexation with polysaccharides. Electrostatic protein-polysaccharide complexes can be formed through electrostatic interactions between oppositely charged biopolymers, depending on, amongst others, pH, ionic strength, and concentration of the protein and polysaccharide. Upon mixing protein and polysaccharides, three possible scenarios may occur (McClements, 2006; Junmiao Zhang et al., 2023). When the pH is close to neutral, both proteins and polysaccharides are mostly negatively charged, which results in strong electrostatic repulsions between both biopolymers and thus co-solubilization of proteins and polysaccharides in the continuous phase. As the pH is reduced to a value lower than the isoelectric points of proteins, the biopolymers are oppositely charged, which results in strong attractive electrostatic interactions between proteins and polysaccharides and promotes the formation of soluble complexes. Insoluble complexes or complex coacervates are formed when the pH is reduced to a value that is far below the isoelectric points of the proteins, as the net charge of the complexes becomes neutral due to the strong attractive electrostatic interactions between biopolymers. When the pH is reduced to an extremely low value, the insoluble complexes dissociate and proteins and polysaccharides become co-soluble again (Aryee & Nickerson, 2012; Klassen & Nickerson, 2012). Soluble protein-polysaccharide complexes, such as rice protein and carboxymethyl cellulose complexes (Wan et al., 2023), soy protein and chitosan/guar gum/gellan gum complexes (Han et al., 2024b), napin-pectin complexes (Schmidt et al., 2010), and whey protein-sodium alginate complexes (Xu et al., 2020), have shown excellent functionality with respect to foaming.

On the molecular level, the electrostatic complexation between proteins and polysaccharides can induce molecular changes in protein secondary structure after complex formation. The loss of protein α-helix structure was observed upon the formation of ribulose diphosphate carboxylase-pectin complexes (Braudo & Antonov, 1993) and β-lactoglobulin-acacia gum complexes (Mekhloufi et al., 2005; Sanchez et al., 2001). This observation was likely explained by the abundance of positively charged amino acid groups in this region, which was reduced due to the electrostatic interactions with negatively charged polysaccharides (Girard et al., 2003). Additionally, the exposed hydrophobic groups in protein molecules might be reduced due to the hydrophobic interactions with polysaccharides (Ghosh & Bandyopadhyay, 2012). As to the polysaccharide, it was reported that the double helix structure of β- and ι-carrageenan was disrupted after electrostatically complexing with β-casein. This loss was explained by the electrostatic interactions between biopolymers preventing the formation of internal hydrogen bonds to stabilize the double helix structures (Burova et al., 2007). On the mesoscopic level, the protein-polysaccharide complexes could form different morphologies depending on the type of polysaccharides (i.e., flexible, or rigid polysaccharide structures). Atomic force microscope (AFM) is a common tool to observe the morphological characteristics of biopolymers in nano-scale (Wang & Nie, 2019). Acacia gum, a flexible polysaccharide, formed linear-like complexes with β-lactoglobulin. Xanthan gum (rigid polysaccharide) formed more compact aggregated complexes with β-lactoglobulin (Turgeon et al., 2007).

In the past few years, there have been some studies discussing the interfacial and emulsifying or foaming properties of electrostatic complexes of protein with different types of polysaccharides (Han et al., 2024b; Han et al., 2024a; Huang et al., 2024). To the best of our knowledge, current research still lacks an understanding of the role of the molecular features of complexes (especially morphological characteristics) in stabilizing food colloidal systems.

In this study, we aim to investigate the role of different morphological characteristics of complexes in stabilizing air-water interfaces and foams. For this purpose, we first chose three polysaccharides (κ-carrageenan, pectin, and sodium alginate) with different chain flexibility to make electrostatic complexes with lupin proteins (1:1 ratio and pH 4.0). The properties of the complexes were determined by dynamic light scattering (DLS), surface hydrophobicity measurement, and atomic force microscopy (AFM). We then systematically investigated the air-water interfacial properties by measuring the adsorption kinetics, interfacial rheology, and interfacial structure. Finally, the foaming properties of the complexes were determined and linked to the air-water interfacial properties.

2. Materials and methods

2.1. Materials

White lupin seeds were purchased from Kamelur (Germany). κ-carrageenan and sodium alginate were purchased from Sigma-Aldrich (USA). Low methoxyl pectin (GENU®, 45CS) was donated by CP Kelco (Atlanta, GA). All other chemicals used in this study were from Sigma-Aldrich (USA). Ultrapure water (MilliQ Purelab Ultra, Germany) was used for all experiments in this study unless stated otherwise.

2.2. Extraction of lupin proteins

Lupin protein isolates (LPI) were extracted by using alkaline dissolving followed by acid precipitation, based on a previous study (Ma, Habibi, et al., 2024a). Briefly, full-fat lupin flour was obtained by initially dehulling the seeds and subsequently milling the seed kernels using a multimill (Hosokawa-Alpine, Augsburg, Germany). Afterward, the full-fat flour was defatted three times using n-hexane (1:10 ratio) at room temperature. The defatted flour was then dispersed in MiliQ water at a 1:10 (w/v) ratio with continuous pH adjustment to 9.0, and the dispersions were subsequently centrifuged at 36,000 g for 10 min to collect the supernatant that contained proteins. The pH of the supernatant was then adjusted to 4.6, and then 90 min was allowed for proteins (i.e., the globulin fraction) to precipitate. Afterward, the protein suspensions were centrifuged at 36,000 g for 5 min to collect the protein pellet containing the globulin fraction, while the supernatant containing mostly albumins was discarded. The globulin fraction was re-dispersed in MiliQ water and the pH was re-adjusted to 7.0. The protein dispersions were dialyzed against MiliQ water for 3 days before freeze-drying.

2.3. Sample preparation

Lupin protein isolates (LPI) and polysaccharide (κ-carrageenan (KC), pectin (PC), and sodium alginate (SA)) stock solutions were prepared at 0.2% (w/w) in MiliQ water. Afterward, LPI-polysaccharide (PC, SA, and KC) mixtures were prepared by mixing 0.2% (w/w) LPI solutions in MiliQ water with 0.2% (w/w) polysaccharide solutions in MiliQ water at a 1:1 (v/v) ratio. Subsequently, electrostatic complexes were obtained by diluting the mixtures in 40 mM pH 4.0 acetate buffer at a 1:1 (v/v) ratio, finally resulting in a 0.1% (w/w) total biopolymer concentration of complex solutions in 20 mM acetate buffer at pH 4.0.

2.4. Determination of particle size distribution and zeta potential

The particle size distribution and zeta potential of LPI-polysaccharide complexes were measured by dynamic light scattering (DLS) using a Zetasizer Nano ZS (Malvern Instruments, UK) according to Ma et al. (2024b). The refractive index of the dispersed and continuous phases was set at 1.450 and 1.330, respectively.

2.5. Determination of surface hydrophobicity

The surface hydrophobicity of LPI and LPI-polysaccharide (LPI-PS) complexes was measured using 8-anilino-1-napthalenesulfonic acid ammonium salt (ANSA) as a fluorescence probe according to Ma, Habibi, et al. (2024b) at room temperature. Stock solutions were initially prepared at 0.1% (w/w) and subsequently diluted to 0.01%, 0.008%, 0.006%, 0.004%, and 0.002%. Afterward, an aliquot (25 μl) of 8 mM ANSA solutions was added to 3 ml of the diluted solutions and 1 h was allowed for reactions. A fluorescence spectrophotometer (Shimadzu RF 6000 Fluorometer) was used to measure the fluorescence intensity at an excitation and emission wavelength of 390 nm and 470 nm, respectively. Acetate buffer (20 mM and pH 4.0) with ANSA was used as blank. The initial slope of fluorescence intensity against solution concentrations was used as a measure for surface hydrophobicity.

2.6. Characterization of complex morphology

Samples were first prepared by droplet-wise depositing 5 μl of 0.01% (w/w) LPI-polysaccharide complex solutions on freshly cleaved mica sheets (Highest Grade V1 Mica, Ted Pella, USA) and subsequently dried in a desiccator at least two days before imaging. The morphology of the complexes was captured by atomic force microscopy (AFM, NanoWizard® 4XP NanoScience, Bruker Nano GmbH, Germany) using the peak force tapping mode with a PEAKFORCE-HIRS-F-A cantilever (Bruker, USA) (spring constant of 0.42 N/m and tip radius of 1 nm) according to Ma, Habibi, et al. (2024b). The scan area for each sample was set at 10×10 μm^2 and 2×2 μm^2 with a line rate of 1.7 Hz and setpoint of 0.5 nN. The raw data were analyzed with the Nanoscope Analysis v1.5 software (Bruker, USA)

2.7. Air-water interfacial adsorption behavior

The air-water interfacial adsorption behavior of LPI and LPI-PS complexes were monitored by a Tracker Automatic Droplet Tensiometer (ADT) (Teclis, France) from 1 s to 10,800 s. Briefly, a rising bubble of 15 mm^2 was formed at the tip of a G16 needle, and then the surface tension of the bubble was continuously monitored by capturing the droplet contour with a camera. The surface tension was then calculated by fitting the shape captured by the camera with the Young-Laplace equation. All measurements were performed at least in triplicate at 20 °C.

2.8. Interfacial shear rheology

After 3h of adsorption, the interfacial shear rheology of the air-water interface was characterized using a stress-controlled MCR 302e rheometer (Anton Paar, Graz, Austria) coupled with a double wall ring (DWR) geometry at room temperature according to Ma, Habibi, et al. (2024b). Briefly, a Teflon double wall trough was first filled with 15 ml of solutions, and then the DWR geometry was positioned at the air-water interface. The air-water interface was subjected to a time sweep (0.1% of strain and 0.1 Hz of frequency) for 3 h, a frequency sweep (0.01 Hz–10 Hz, at a fixed strain of 1%), and a strain sweep (0.01%–100% of strain at a fixed frequency of 0.1 Hz) in sequence. The results from the strain sweeps were then extracted to construct Lissajous plots, while the frequency sweep data were fitted with a power law equation ($G' \sim \omega^n$, where G' is the storage modulus, ω is frequency, and n is the power law exponent) to obtain the exponent, n.

2.9. Interfacial dilatational rheology

Interfacial dilatational rheology was performed using a Tracker Automatic Droplet Tensiometer (ADT) (Teclis, France) at 20 °C. Firstly, time sweeps were conducted at a frequency of 0.02 Hz and an amplitude of 3%. After 3h of adsorption, a frequency sweep was performed at a frequency from 0.005 Hz to 0.1 Hz and a fixed amplitude of 3%. The results from the frequency sweep were then used to fit a power law model ($E_d' \sim \omega^m$, where E_d' is the dilatational elastic modulus and ω is the frequency) to calculate the exponent, m. Amplitude sweeps were then conducted at amplitudes from 3% to 50% and a fixed frequency of 0.02 Hz. Five cycles were performed in the amplitude sweeps and the middle three cycles were used to construct Lissajous plots. These Lissajous plots were further analyzed with the general stress decomposition (GSD) according to de Groot et al. (2023).

2.10. Preparation of Langmuir-Blodgett films

Langmuir-Blodgett (LB) films were prepared using a Langmuir trough (KSV NIMA/Biolin Scientific, Finland) based on a previous study (Ma et al., 2024). Briefly, the trough was initially filled with around 200 ml of clean 20 mM pH 4.0 acetate buffer, and subsequently a freshly cleaved mica sheet was immersed into the buffer before injecting 1–4 ml of protein/complex solutions at the bottom of the trough. After 3 h of adsorption, the Teflon barriers were moved at a speed of 5 mm/s to compress the air-water interface until reaching a target surface pressure of 10 mN/m or 20 mN/m. Afterward, the mica sheet was lifted at a speed of 1 mm/s while keeping the target surface pressure constant by moving the Teflon barriers. These LB films were prepared in duplicate and dried in a desiccator at least 2 day at room temperature before further analysis.

2.11. Characterization of air-water interfacial structures by AFM

The air-water interfacial structures were analyzed by imaging the LB films with atomic force microscopy (NanoWizard® 4XP NanoScience, Bruker Nano GmbH, Germany), following the same procedure as in Section 2.6. These AFM images were further quantitatively analyzed with Angiotool 64 software (National cancer Institute, National Institute of Health, Maryland, USA). Briefly, vessel area, vessel percentage area, junction density, average vessel length, end-point rate, branching rate, and mean lacunarity were calculated by the software to characterize the protein network at the air-water interface (Bernklau et al., 2016; Munialo et al., 2015).

2.12. Determination of foaming properties

Foamability and foam stability of LPI and LPI-PS complexes were measured at room temperature according to a previous study (Ma, Habibi, et al., 2024a). Briefly, the foamability was measured by whipping 15 ml of sample solutions in a plastic cylinder tube at 2000 rpm for 2 min, using an overhead stirrer connected to an Aerolatte froth (Aerolatte, UK). The foam overrun (%) was calculated as foam height (cm)/initial liquid height (cm). The foam stability was measured using the gas sparging method. A glass cylinder was initially filled with 40 ml of sample solution, followed by sparging the solutions with N_2 gas until reaching a foam volume of 60 cm^3. Foam and liquid height were continuously monitored during foam aging to calculate foam half-life time. The bubble size of the foams was measured using two transparent Plexiglas plates (Ma, Shen, et al., 2024). The freshly prepared foams were initially transferred to the gap (0.26 mm) between the Plexiglas plates, and subsequently, the foam morphology was captured by a high-resolution camera. The 2D images of the foams were analyzed with ImageJ, which were then converted to equivalent 3D spherical

volumes (Area × gap) to calculate the average bubble size. Examples of 2D foam images and bubble size distributions are shown in Supplementary Information (SI).

2.13. Statistical analysis

One-way ANOVA followed by Tukey's tests was conducted by Origin 2021 to compare samples using a significance level of 0.05.

3. Results and discussion

3.1. Physiochemical properties of lupin protein-polysaccharide complexes

The particle size distributions and zeta potential of LPI in 20 mM pH 4.0 acetate buffer/MiliQ water and LPI-polysaccharide (LPI-PS) complexes are shown in Fig. 1(A and B). The soluble fractions of LPI at pH 4.0 (LPI-4) showed a monomodal distribution with a peak around 11.2 nm, while the full fraction of LPI in MiliQ water (LPI-MQ) showed a bimodal distribution with the first peak at 37.6 nm and the second peak at 197.6 nm. The reduction of protein particle size at pH 4.0 was due to the precipitation of large protein aggregates as a result of reduced protein solubility at acidic pH. LPI-PS complexes showed similar bimodal distributions as the full fractions of LPI in MiliQ water. Presumably, the first and second peaks may correspond to free proteins (e.g., individual proteins and small protein clusters) and LPI-PS complexes, respectively. LPI-SA complexes showed a comparable distribution to LPI-MQ, while LPI-KC and LPI-PC complexes showed a shift to larger sizes of both the first and second peaks compared to LPI-MQ. This indicates that LPI-KC (~488.7 nm) and LPI-PC (~267.2 nm) had larger particle sizes than LPI-SA complexes (~197.6 nm). Regarding the zeta potential, all complexes showed highly negative charges (absolute values larger than 30 mV), while LPI-4 was positively charged with a value of around 16 mV.

Surface hydrophobicity (H_0) can reflect changes in protein conformation as a result of the electrostatic complexation of proteins with polysaccharides. As shown in Fig. 1C, all LPI-PS complexes showed significantly lower H_0 values than LPI-4, indicating a reduction in exposed hydrophobic groups of the protein due to the formation of electrostatic complexes. Among LPI-PS complexes, LPI-KC complexes showed a slightly lower H_0 value (0.47 ± 0.01) than LPI-PC (0.54 ± 0.00) and LPI-SA (0.56 ± 0.01). This may indicate that there are slightly more hydrophobic interactions between LPI and KC and thus more surface hydrophobic groups were buried, resulting in a lower H_0 value than LPI-PC and LPI-SA complexes.

3.2. Morphological characteristics of lupin protein-polysaccharide complexes

Atomic force microscopy (AFM) was used to examine the morphology of LPI-KC, LPI-PC, and LPI-SA complexes (Fig. 2). For the LPI-KC complexes, we observed a large, aggregated structure (500–600 nm), consisting of several chain molecules and large globular protein clusters, forming a highly cross-linked structure, apparently cross-linked by individual proteins and small protein clusters. Regarding the LPI-PC complexes, their structure seems to be more compact and less branched than the LPI-KC complexes. Their structures mostly consisted of a dense core (100–300 nm) with multiple protruding pectin chains; therefore, the structure appeared to be more core-shell-like. LPI-SA complexes were composed of sodium alginate chains bound by several protein molecules and had a more linear structure with less structural cross-linking than LPI-KC and LPI-PC.

The structure and strength of protein-polysaccharide complexes depend on the physiochemical properties of both biopolymers, such as the charged groups of the proteins, the molecular flexibility of the native proteins (i.e., the ease of the structural unfolding), the chain flexibility, and the charge distributions on the polysaccharide backbones (Ledward, 1994, pp. 225–259). The different morphological characteristics across LPI-KC, LPI-PC, and LPI-SA complexes could be attributed to the chain flexibility of the polysaccharides. The linear chain flexibility of polysaccharides is commonly described by their persistence length (L_p), defined as the length over which the polymer chain maintains its directional persistence (Buhler & Boue, 2004). A perfect random coil structure has $L_p = 0$, while a rigid rod has $L_p = \infty$ (Harding, 1997; Harding et al., 2017). The persistence length of κ-carrageenan is in the range of 60–90 nm in 0.1 M salt solutions (Borgström et al., 1998), significantly higher than pectin, with an L_p in the range of 10–15 nm in 0.1 M salt solutions (G. Morris et al., 2000; G. A. Morris et al., 2008) and sodium alginate with an L_p of 4.1–5.1 nm at 0.1 M salt (Banerjee, De, & Das, 2022). These results indicated that κ-carrageenan has a much more rigid molecular structure (i.e., double helix structure) (Campo et al., 2009), while pectin and sodium alginate formed a semi-flexible and flexible structure, respectively (Qiu et al., 2019).

It should be noted that the non-covalent interactions between protein reactive groups (e.g., amine, carboxyl, hydroxyl, and thiol groups) and polysaccharide reactive groups (e.g., sulfate/hydroxyl groups in κ-carrageenan, carboxyl/methyl ester groups in pectin, and carboxyl/hydroxyl groups in the sodium alginate) can occur through electrostatic interactions, hydrogen bonding, and hydrophobic interactions (Han et al., 2024a). At acidic pH, the protein-polysaccharide complexes were mainly stabilized by electrostatic interactions, but when the biopolymers come in contact, junction zones between biopolymers might also be formed through hydrogen bonding and hydrophobic interactions

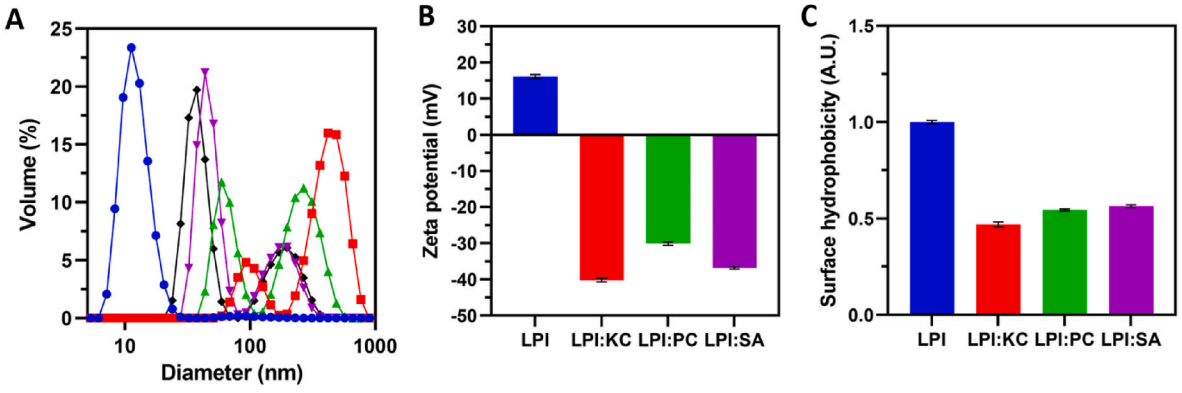

Fig. 1. (A) Volume-based particle size distribution of lupin protein at pH 4.0 (—●—), lupin protein in MiliQ water (—◆—), LPI-KC complexes (—■—), LPI-PC complexes (—▲—), and LPI-SA complexes (—▼—). Zeta potential (B) and relative surface hydrophobicity (C) of lupin protein at pH 4.0, LPI-KC complexes, LPI-PC complexes, and LPI-SA complexes.

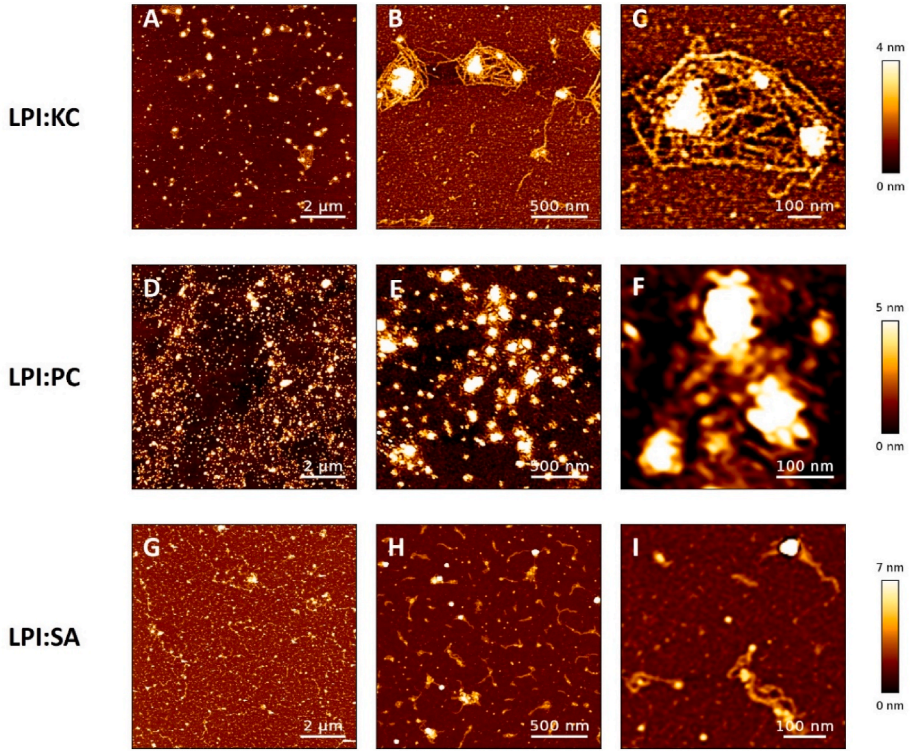

Fig. 2. Complex morphological characteristics (imaged with AFM) of LPI-KC complexes (A–C), LPI-PC complexes (D–F), and LPI-SA complexes (G–I).

(Schmitt et al., 1998; Schmitt & Turgeon, 2011). In principle, covalent bonds can also be formed between protein molecules and between proteins and polysaccharides in mixed systems under certain conditions, such as by oxidation and Maillard reactions. Protein-protein interactions occur faster due to higher diffusivity and accessibility of reactive groups, while protein-polysaccharide interactions are slower due to the large molecular weight and steric hindrance of polysaccharides. But at acidic pH (i.e., lower than pI), the proteins and polysaccharides are oppositely charged, and attractive electrostatic interactions between proteins and polysaccharides are more favorable over protein-protein interactions (Koren & Hammes, 1976; Schmitt et al., 1998; Jing Zhang & Liu, 2003).

Due to the rigidity of κ-carrageenan, it is unable to easily bend or twist its structure and wrap itself around the surface of the proteins. Instead, it may locally interact with proteins at a single specific binding point (i.e., the polymeric chains become tangent to the globular protein molecules) (Akinchina & Linse, 2002; Stoll & Chodanowski, 2002). Protein surfaces have multiple active binding sites, which could allow multiple κ-carrageenan chains to interact with the protein. When multiple κ-carrageenan chains come together and interact with the same protein molecules, it may result in the cross-linking of these chains and form a highly interconnected network. The resulting LPI-KC complexes were also larger (~488.7 nm) than LPI-PC (~267.2 nm) and LPI-SA (~197.6 nm), and this could also be a consequence of the longer persistence length of this polysaccharide. As to pectin, due to its semi-flexible nature, it may associate with protein surfaces more extensively than KC (Akinchina et al., 2002; Stoll et al., 2002) and form denser cross-linked structures. In contrast, the flexible sodium alginate may have even more conformational freedom to rearrange its structure to associate with the reactive sites on the protein surface (Doublier et al., 2000; Stoll et al., 2002; Turgeon et al., 2003). As a result, sodium alginate could easily wrap around and extend its structures along the protein surface, which reduces the active sites on the protein surfaces and thus limits more sodium alginates from interacting with the same protein molecules. This resulted in reduced cross-linking and the formation of a more linear complex. In view of the chain flexibility of these polysaccharides, LPI-KC may form the most rigid structures due to the rigid structure of κ-carrageenan and its highly cross-linked structure. While LPI-PC may have a more flexible structure due to the semi-flexible nature of pectin chains. LPI-SA is likely to have the most flexible structure as a result of the flexibility of sodium alginate and its open structure with less cross-linking.

3.3. Air-water adsorption kinetics of LPI-polysaccharide complexes

The adsorption behavior of LPI, LPI-KC, LPI-PC, and LPI-SA at the air-water interface is shown in Fig. 3A. The surface pressure of LPI already increased to around 10 mN/m at 1 s, while LPI-PS clearly showed a lag time ranging from 3 s to 15 s. This indicates that LPI diffused faster to the interface than LPI-PS, due to the smaller particle size of proteins. Amongst LPI-PS complexes, LPI-KC showed the slowest diffused rate, since the LPI-KC had larger particle sizes and lower surface hydrophobicity than LPI-PC and LPI-SA, which reduced its affinity to the air-water interface. LPI-PC and LPI-SA showed a comparable adsorption rate, even if LPI-PC had a slightly larger particle size (~267.2 nm) than LPI-SA (~197.6 nm). Considering LPI-PC had a lower zeta potential (−29.9 mV) than LPI-SA (−36.0 mV), the lower charge of LPI-PC may reduce the energy barrier for adsorption at the air-water interface, which finally resulted in a comparable adsorption rate with LPI-SA. After 3 h of adsorption, LPI, LPI-PC, and LPI-SA reached a relatively higher surface pressure than LPI-KC. The differences in the quasi-equilibrium surface pressure might be caused by the structural rearrangement at the air-water interface (Wierenga et al., 2003). LPI-KC had a more rigid structure due to the rigid chains of κ-carrageenan than LPI-PC and LPI-SA, which may cause a lower degree of structural rearrangement at the air-water interface and result in a lower quasi-equilibrium surface pressure.

To monitor the development of the air-water interface of LPI and LPI-PS during adsorption, we conducted interfacial shear and dilatational time sweeps as shown in Fig. 3(B and C). In the initial adsorption stages (i.e., the first point in both plots), LPI-KC already developed significantly higher G′ and E_d' values (G' = 28.0 ± 4.0 mPa m and E_d' = 49.2 ± 3.0 mN/m) than LPI-PC (7.9 ± 2.3 mPa m and 20.6 ± 0.6 mN/m), LPI (6.1

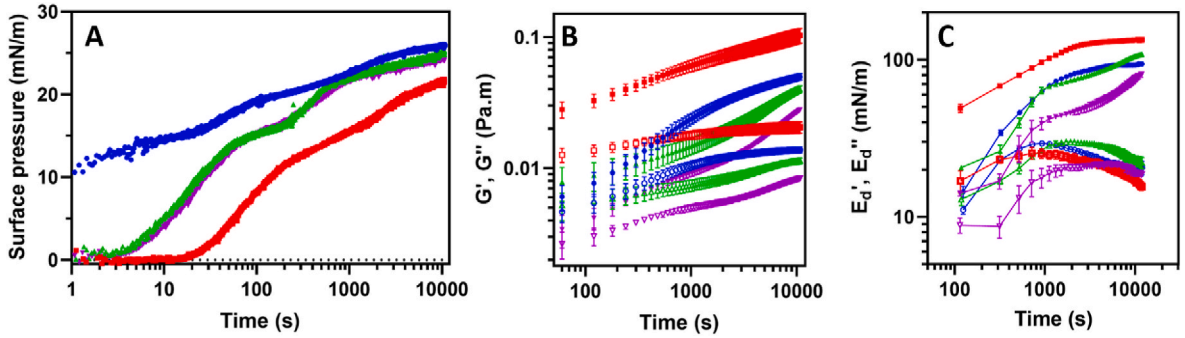

Fig. 3. The development of surface pressure (A), interfacial shear modulus (G′ and G′′) (B), and interfacial dilatational modulus (E_d' and E_d'') (C) as a function of time for LPI (●), LPI-KC complexes (■), LPI-PC complexes (▲), and LPI-SA complexes (▼). G′ and E_d' are denoted by closed symbols, G'' and E_d'' by open symbols. In the shear time sweep strain was equal to 0.1% and frequency was 0.1 Hz; dilatational time sweeps were performed at 3% strain and 0.02Hz.

± 1.3 mPa m and 14.4 ± 1.2 mN/m), and LPI-SA (3.4 ± 1.0 mPa m and 14.1 ± 0.5 mN/m), indicating that LPI-KC could form a stiffer air-water interface in the early adsorption stage, despite its longer lag time.

After the initial adsorption phase, LPI-KC showed a gradual increase of the dilatational moduli up to about 2000 s, and then the moduli level off from 2000 s onwards (Fig. 3C). In shear rheology (Fig. 3B), the moduli of LPI-KC continuously increased with time during the adsorption, without any clear transition phases, as seen in Fig. 3B. Since there is no visible slope change in the curve of G' around 2000 s, and only a minor change of slope in the adsorption curve (Fig. 3A), the slope change in the dilatational curve is most likely not the result of rearrangement processes, but rather caused by disruption of the microstructure of the interface by the applied deformation. As we will show in the strain sweeps (Fig. 6), the 3% strain we applied during the adsorption stage is already in the nonlinear regime, and hence may have affected structure formation.

LPI-PC and LPI-SA showed a gradual increase of moduli up to 1000 s in both shear and dilatational deformation, and then displayed an upswing in both curves after 1000 s, indicating that LPI-PC and LPI-SA had a faster increase of the moduli of the air-water interface during the latter stages of adsorption than LPI-KC. The fact that both curves show an increase in the rate of modulus development, indicates that this is likely caused by late-stage rearrangement processes, which lead to increased density and network interactions. These different observations could result from differences in the molecular flexibility of the LPI-PS complexes. LPI-KC had a rigid molecular structure, which may limit its structural rearrangement at the later stages of adsorption. In contrast, LPI-SA had more flexibility than the rigid LPI-KC and the semi-flexible LPI-PC, which may facilitate the rearrangement of its structure and result in the faster growth rate of the interface in the later adsorption stages.

3.4. Interfacial rheology of LPI-polysaccharide complexes

3.4.1. Interfacial shear rheology

After 3 h of adsorption, the air-water interface was subjected to interfacial shear frequency sweeps (Fig. 4A). The G′ values of LPI and all LPI-PS complexes were larger than the G'' values, indicating the formation of solid-like air-water interfaces at the applied frequency ranges. All LPI and LPI-PS complexes showed a low-frequency dependency, with power-law exponents n in the range of 0.12–0.18 (Fig. 4B), implying the formation of soft disordered solid structures at the air-water interface with a wide spectrum of relaxation times, which is typical for gel and soft glassy materials (Jaishankar & McKinley, 2013; Winter & Mours, 1999). Besides, LPI-KC showed a significantly lower *n* value ($p < 0.05$) than LPI, LPI-PC, and LPI-SA, indicating lower frequency dependency. This observation could be attributed to the rigid structure of LPI-KC, which reduced its in-plane mobility.

We then performed strain sweeps of LPI and LPI-PS stabilized air-water interfaces with strains ranging from 0.1% to 100% and a fixed

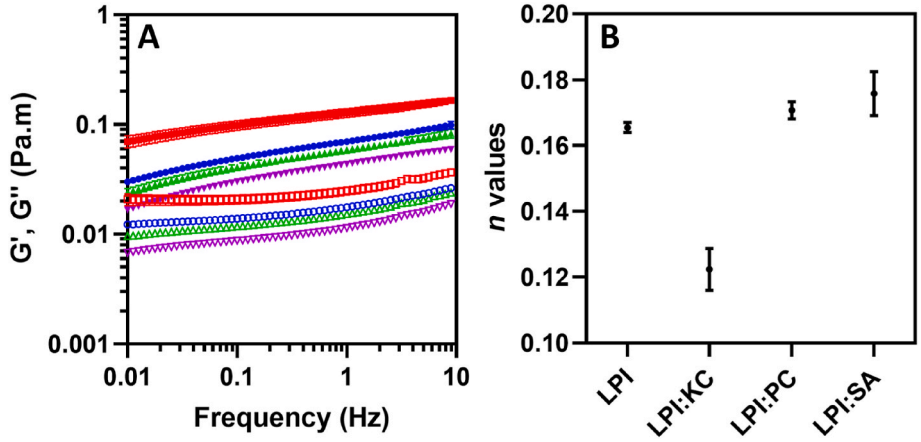

Fig. 4. (A) The interfacial shear elastic modulus (G′) and loss modulus (G'') of LPI, LPI-KC, LPI-PC, and LPI-SA as a function of frequency (Hz). (B) The exponents (*n* values) obtained from the power law equation $G' \sim \omega^n$ for LPI (● and ○), LPI-KC (■ and □), LPI-PC (▲ and △), and LPI-SA (▼ and ▽). The filled and open symbol represents interfacial shear storage and loss modulus, respectively.

frequency of 0.1 Hz (Fig. 5A). In the low strain ranges (lower than 2%), all interfaces showed independence of G′ values on applied strains, representing the linear viscoelastic (LVE) regimes. In the LVE regime, LPI-KC clearly showed a higher G′ value (107.7 ± 10.2 mPa m) than LPI (53.2 ± 2.9 mPa m), LPI-PC (45.8 ± 2.1 mPa m), and LPI-SA (34.0 ± 1.1 mPa m), indicating LPI-KC formed the stiffest air-water interface among these samples in the LVE regime. As the strain further increased beyond the LVE regime, the G′ and G'' values of all interfaces started to decrease until a cross-over point. Beyond this cross-point, the G′ values were lower than the G'' values, indicating the dominance of liquid behavior of the interface due to the disruption of the interfacial microstructure at large shear deformation. LPI (20.1%) and LPI-KC (20.1%) clearly had higher cross-over points than LPI-SA (12.7%) and LPI-PC (11.3%), indicating that LPI and LPI-KC showed solid-like behaviors over a wider range of strains in the NLVE regime than LPI-SA and LPI-PC.

To further investigate the LVE and NLVE behavior of LPI and LPI-PS, we constructed normalized Lissajous plots at strains from 0.5% to 100% (Fig. 5B). At a strain of 0.5% (within the LVE regime), all Lissajous plots were elliptical and narrow with predominantly elastic contributions. When the strain increased from 0.5% to 16%, the Lissajous plots became wider and distorted, indicating increased viscous contributions to the shear stress due to the disruption of the interfacial microstructure. At this strain, LPI showed the least distortion from an elliptical shape, and LPI-PC and LPI-SA showed the most distortion, pointing to a more significant degree of disruption of the interfacial structure. At 100% strain, the Lissajous plots of LPI and LPI-KC were almost rhomboidal but still had a significant elastic component, indicated by the finite slope of the curve of the elastic contribution (red curve) around zero intracycle strain. In contrast, the plots for LPI-PC and LPI-SA were almost rectangular with nearly zero slopes for the decomposed elastic stress lines around zero strain, implying that the interfacial structures of LPI-PC and LPI-SA had almost completely yielded at 100% strain. To quantitatively analyze these Lissajous plots, the dissipation ratio of these plots was calculated (Fig. 5C). In the LVE regimes (lower than 1% strain), the dissipation ratio for all interfaces was smaller than 0.2, suggesting the dominance of elastic behavior over viscous behavior. In the NLVE regimes, all interfaces showed a dramatic increase in the dissipation ratio with the increased strains, indicating the increased viscous behavior at the large strains due to the disruption of the interfacial structure. At 100% strain, LPI and LPI-KC showed a significantly lower ($p < 0.05$) dissipation ratio than LPI-PC and LPI-SA, indicating that LPI-PC and LPI-SA stabilized interfaces had more viscous behavior than LPI and LPI-KC.

Overall, LPI-KC formed a stiffer air-water interface than LPI, LPI-PC, and LPI-SA in response to smaller shear deformation. In the NLVE regime, the LPI and LPI-KC stabilized interfaces were more resistant to large shear deformations than LPI-PC and LPI-SA. These phenomena could result from the more rigid structure of LPI-KC making it more resistant to be disrupted under the large shear deformation. According to a previous study (Ma, Shen, et al., 2024), LPI formed a more jammed particulate air-water interface dominated by small protein clusters, while LPI-PC may form more polymeric interfaces as a result of the pectin chains protruding from its core which may entangle at the interface. The flexible linear complexes of LPI-SA are also likely to have a more polymeric behavior. Thus, the polymeric nature of the LPI-PC and LPI-SA disruption of the interfacial microstructure is most likely the result of disentanglement, whereas for the densely packed LPI particle interface disruption of clusters is a more likely mechanism (Ma, Shen, et al., 2024), resulting in more soft plastic behaviors of LPI-PC and LPI-SA at large deformations. LPI-KC, as a result of its rigidity, may also behave more like a particle network. The particle-like behavior of LPI-KC interfaces could be also indicated by a slight overshoot in the G'' curve around 3% (known as the Payne effect), which is often observed for particle network systems (Giménez-Ribes et al., 2023; Hyun et al., 2002).

3.4.2. *Interfacial dilatational rheology*

The interfacial dilatational rheology including frequency and amplitude sweeps was conducted after 3 h of adsorption. In the frequency sweep (Fig. 6A), the elastic modulus (E_d') of all interfaces showed a weak frequency dependence, described well by a power law ($E_d' \sim \omega^m$, where E_d' was dilatational storage modulus, ω is the

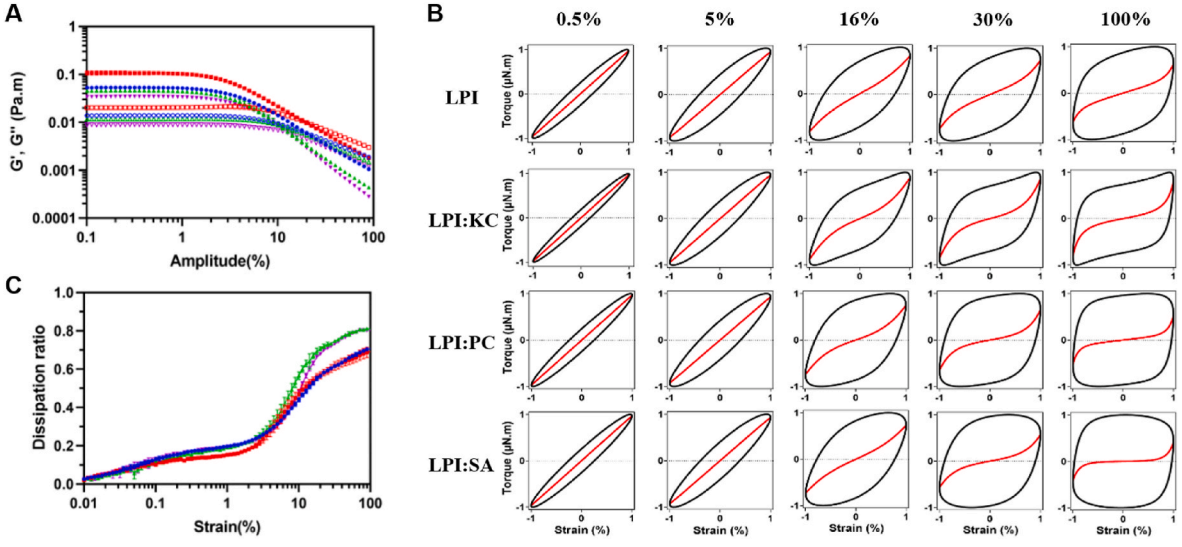

Fig. 5. (A) The interfacial elastic modulus (G′) and loss modulus (G'') of LPI (● and ○), LPI-KC (■ and □), LPI-PC (▲ and △), and LPI-SA (▼ and ▽) as a function of strain (%). (B) Normalized Lissajous plots (black curve) and decomposed elastic components (red curve) of LPI, LPI-KC, LPI-PC, and LPI-SA at a strain ranging from 0.5% to 100%. (C) Dissipation energy ratio of the Lissajous plots of LPI (●), LPI-KC (■), LPI-PC (▲), and LPI-SA (▼).

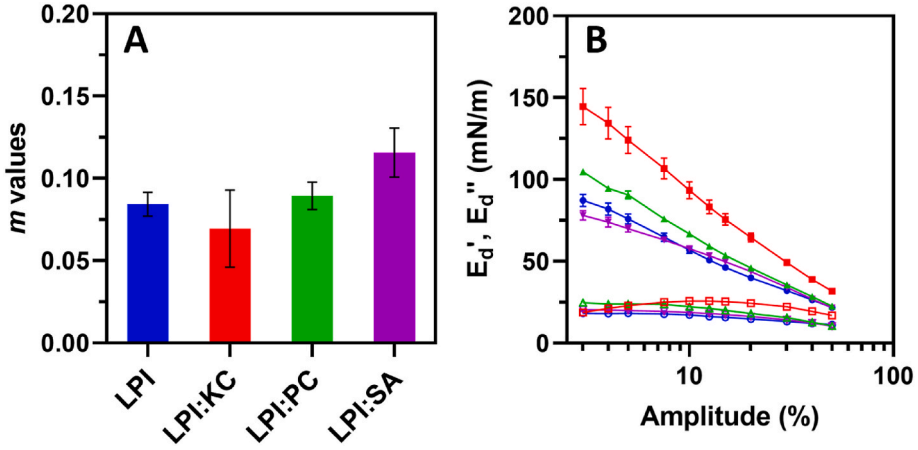

Fig. 6. (A) The power law exponent (*m* value) of LPI, LPI-KC, LPI-PC, and LPI-SA obtained from the interfacial dilatational frequency sweep at a fixed amplitude of 3%. (B) The dilatational elastic (E_d') and viscous (E_d'') modulus of LPI (—●— and —○—), LPI-KC (—■— and —□—), LPI-PC (—▲— and —△—), and LPI-SA (—▼— and —▽—) as a function of amplitude (3–50%) at a fixed frequency of 0.02 Hz. The filled and open symbol represents interfacial dilatational storage and loss modulus, respectively.

frequency, and m is the power law fitting exponent), with m values ranging from 0.07 to 0.12. An *m* value obtained from dilatational frequency sweeps of 0.5, suggests that the response of the interface to the applied dilatational deformation is mainly dominated by the exchange of interfacial stabilizer between bulk and interfaces (Lucassen & Van Den Tempel, 1972). In our case, all interfaces clearly showed an m value significantly smaller than 0.5, indicating that all interfaces had low exchangeability of the interfacial materials between bulk and interfaces and formed soft disordered solid-like air-water interfaces, consistent with the interfacial shear results, where we observed exponents in the range of 0.12–0.18.

In amplitude sweeps (Fig. 6B), all interfaces showed larger elastic modulus (E_d') than viscous modulus (E_d'') over the entire amplitude ranges, indicating the formation of viscoelastic solid-like air-water interfaces. At the small deformation of 3%, LPI-KC had the largest E_d' value (144.6 ± 11.0 mN/m), followed by LPI-PC (104.8 ± 1.0 mN/m) and LPI (87.3 ± 3.8 mN/m), while LPI-SA had the smallest value of E_d' (78.1 ± 2.8 mN/m). These results indicated that LPI-KC formed the stiffest air-water interfaces with the strongest in-plane interactions (i.e., the molecular interactions between LPI-KC complexes adsorbed at the air-water interface). When amplitudes are increased, the E_d' values of all interfaces are reduced due to the disruption of the interfacial structure. It should be noted that LPI-KC still had a pronouncedly higher E_d' value at 50% deformation (~32.0 mN/m) than LPI, LPI-PC, and LPI-SA (~22.0 mN/m), indicating that LPI-KC had more residual elasticity at 50% deformation than the rest of interfaces.

To further analyze the non-linear behavior of LPI, LPI-KC, LPI-PC, and LPI-SA stabilized interfaces, we constructed Lissajous plots at amplitudes ranging from 5% to 50% (Fig. S1). At 5% deformations, all plots showed elliptical and narrow shapes, indicating a predominantly elastic behavior. With increasing amplitudes from 10% to 50%, these plots started to become wider and asymmetric, suggesting the increased viscous behaviors of these interfaces. At 50% deformation, the plot first started with a steep slope (the left corner of the plot) at the start of the expansion, indicating a high initial interfacial stiffness. When further expanding the interface, the slopes of the interface were gradually reduced, due to the disruption of the interfacial structure and the decrease in interfacial density, which resulted in the strain softening of the interface. Upon compression of the interface, the increased surface density caused the jamming of the interface, resulting in strain hardening. For the Lissajous plots at 50%, LPI-KC had more strain-hardening but less strain-softening than LPI, LPI-PC, and LPI-SA, suggesting that LPI-KC stabilized interfaces were more resistant to surface density and network structure changes in compression and expansion of the interface. In the next section, we further separated the non-linear behaviors in these Lissajous plots into network contributions and surface density contributions using the general stress decomposition (GSD) method (de Groot et al., 2023).

3.4.3. *General stress decomposition*

To analyze the non-linearities of Lissajous plots in Fig. S1, we applied the general stress decomposition (GSD) to separate the stress response in these plots into odd and even harmonics, which correspond to network disruptions and surface density changes, respectively. The odd harmonics consist of both elastic (τ_1) and viscous (τ_2) components, and the even harmonics also include energy dissipation (τ_3) and storage (τ_4) contributions.

The decomposed plots of LPI, LPI-KC, LPI-PC, and LPI-SA at 50% deformation are shown as an example in Fig. S2. Focusing on the odd harmonics (Fig. S2 B1-B4), we see that the curves for $\tau_1 + \tau_2$ (red curves) for LPI, LPI-PC, and LPI-SA, are still near elliptical, with nearly straight elastic components (blue line), whereas for LPI-KC the curve has taken on a rhomboidal shape, indicating the interfacial microstructure has partially yielded. The elastic component still has the highest slope of all four samples, and even shows a mild degree of strain hardening towards maximum expansion/compression. This again indicates that LPI-KC forms a much stiffer air-water interface. Regarding the viscous component of the odd harmonics, LPI-KC also showed a significantly wider τ_2 loop than the other interfaces (Fig. S2 C1-C4), implying LPI-KC had more energy dissipation due to the network disruption. Regarding the even harmonics (Fig. S2 D1-D4), they show a single downward curve (τ_4) and a lemniscate loop (τ_3), representing the elastic and viscous components, respectively. LPI and LPI-KC clearly showed more negative shifts with respect to the horizontal axis of the τ_4 curve and a wider τ_3 loop than LPI-PC and LPI-SA, suggesting more contributions from surface density changes.

We further characterized these plots by calculating several GSD parameters (Fig. 7). The $E_{\tau 1L}$ modulus (the secant modulus, equal to the slope of the line connecting the origin with the value of τ_1 at maximum expansion, and representing interfacial stiffness) of all interfaces was reduced with increasing deformation (Fig. 7A), indicating the disruption of interfacial structure at large deformation. LPI-KC showed the highest values for the $E_{\tau 1L}$ modulus, followed by LPI-PC and LPI, while LPI-SA showed the lowest value. This result indicated that LPI-KC formed the

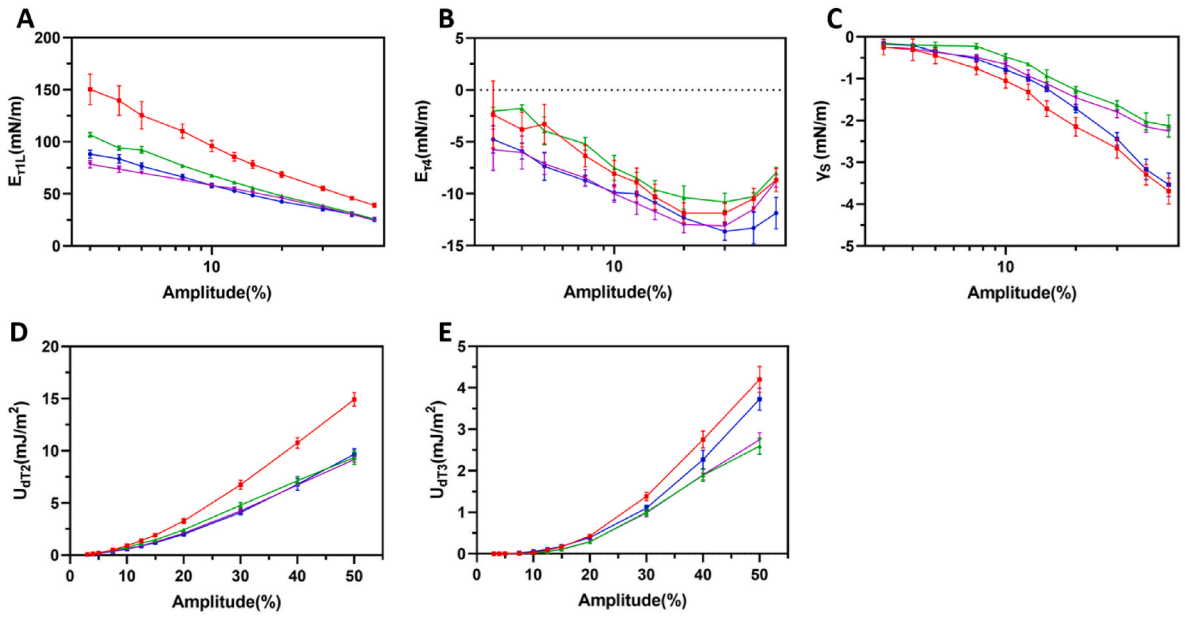

Fig. 7. Quantitative GSD parameters ($E_{\tau 1L}$, $E_{\tau 4}$, Υ_s, $U_{d\tau 2}$, and $U_{d\tau 3}$) for LPI (—●—), LPI-KC (—■—), LPI-PC (—▲—), and LPI-SA (—▼—) stabilized air-water interface as a function of amplitude.

stiffest air-water interface, while LPI-SA formed the weakest interface. The LPI-KC stabilized interfaces also showed a significantly higher value of $U_{d\tau 2}$ (the area within the loop enclosed by τ_2, and a measure for the energy per cycle dissipated through network disruption) than other interfaces (Fig. 7D), indicating that the stiffer interfaces formed by LPI-KC required more energy to disrupt and that the in-plane interactions between the LPI-KC were significantly stronger than between the other components.

The contributions from even harmonics were shown in Fig. 7B, 7C, and 7E. LPI showed a slightly higher $E_{\tau 4}$ modulus (the absolute value of the slope of the line connecting the center of τ_4 with its value at maximum expansion) (Fig. 7B) than LPI-KC, LPI-PC, and LPI-SA at 30%, 40%, and 50% deformation, implying that the surface density had a more significant contribution in the LPI-stabilized interfaces to the total stress response. The vertical shift (γ_s) of the τ_4 curve is a measure for how far the system was driven out of equilibrium by the oscillations. All interfaces showed a more negative γ_s value with increasing amplitudes. The γ_s values of LPI-KC and LPI clearly were significantly more negative than those of LPI-PC and LPI-SA, implying a slower in-plane relaxation of the LPI-KC and LPI stabilized interfaces. This might be due to the formation of densely packed interfaces, which limited the in-plane mobility and thus caused slow restoration of the interface to the equilibrium states at zero intracycle strain. LPI-PC and LPI-SA had a more flexible structure, which may facilitate their structural rearrangement and result in faster in-plane relaxations. The LPI and LPI-KC stabilized interfaces also showed higher energy dissipation as a result of surface density changes ($U_{d\tau 3}$) than LPI-PC and LPI-SA (Fig. 7E), which again indicated the formation of denser interfaces for LPI and LPI-KC.

Overall, the LPI-KC stabilized interface had more pronounced contributions from the odd and even harmonics and thus formed a stiffer and denser air-water interface than LPI-PC and LPI-SA. Meanwhile, the LPI-KC stabilized interface had more contributions from odd harmonics than LPI, but it showed a comparable contribution from the even harmonics. These observations could be caused by differences in the interfacial structures formed by LPI, LPI-KC, LPI-PC, and LPI-SA. In the next section, we will use AFM on Langmuir Blodgett films to characterize the interfacial structures formed by these samples.

3.5. *Interfacial structure of LPI-polysaccharide complexes*

To determine the air-water interfacial structure of LPI and LPI-PS, we prepared Langmuir-Blodgett (LB) films at a surface pressure of 10 mN/m and 20 mN/m, and then imaged these with AFM. We subsequently quantitatively analyzed these AFM images at a surface pressure of 20 mN/m. AngioTool was used to perform the image analysis to calculate parameters, such as vessel percentage area, junction density, average vessel length, branching rate, end point rate, and mean lacunarity. Vessel percentage area refers to the percentage of area occupied by the protein/complex network. Junction density (calculated by the number of junction points in the protein network divided by the total area) represents the connectivity of the protein network. Average vessel length describes the average length of threads in the network. Mean lacunarity is calculated by the average number of gaps in the network, and is related to the network heterogeneity (Bernklau et al., 2016; Munialo et al., 2015).

LPI-PS complexes showed completely different air-water interfaces from LPI (Fig. 8). At a surface pressure of 10 mN/m, the LPI stabilized interfaces were mainly dominated by small protein clusters, and appeared to be more homogeneous and denser than those stabilized by LPI-PS. In the AFM micrographs of LPI-PS, we observed several nearly spherical bright regions with diameters up to a few hundred nanometers, which may correspond to the large protein clusters as indicated in Fig. 2. These large protein clusters were surrounded by many long-chain-like structures that were most likely polysaccharides, implying the formation of more polymer-like interfaces. We further compressed the interface to a surface pressure of 20 mN/m, which is close to the equilibrium surface pressure as measured by ADT in Fig. 3A. Qualitatively, these AFM images, especially those of LPI-PS, were significantly denser than those at the surface pressure of 10 mN/m. To obtain quantitative information, we further performed image analysis of these images by AngioTool (Fig. 9). The LB films of LPI-KC showed a higher vessel percentage area and lower end-point rate than those of LPI, LPI-PC, and LPI-SA. They also showed a higher junction density, longer average vessel length, and lower lacunarity than those of LPI, LPI-PC, and LPI-SA, indicating that LPI-KC formed denser, more finely structured interfaces with higher connectivity and longer network threads. LPI and LPI-PC displayed higher vessel percentage area, higher junction density, longer average vessel length, lower end point rate, and lower lacunarity

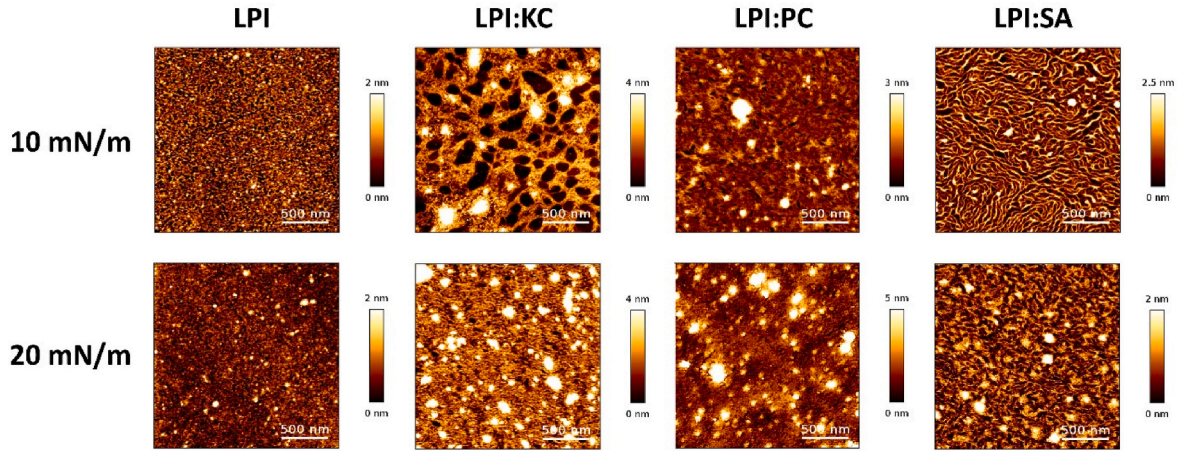

Fig. 8. AFM images of Langmuir-Blodgett films of LPI, LPI-KC, LPI-PC, and LPI-SA at a surface pressure of 10 mN/m and 20 mN/m.

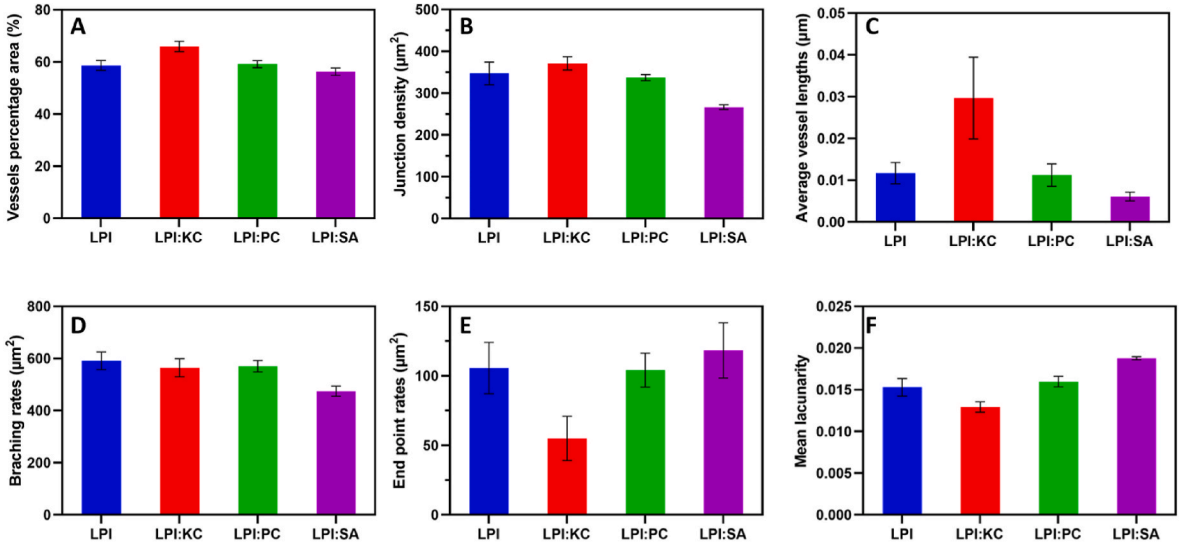

Fig. 9. Image analysis of AFM images at a surface pressure of 20 mM/m, as determined by AngioTool. (A) Vessel percentage area (%); (B) Junction density (μm^2); (C) Average vessel length (μm); (D) Branching rate (μm^2); (E) End point rate (μm^2); (D) Mean lacunarity.

than LPI-SA, indicating LPI and LPI-PC formed denser and finer interfaces with higher connectivity than LPI-SA.

Based on the above information, we can make an overall summary of the interfacial structure in connection with the interfacial mechanical properties. LPI-SA tended to form coarser interfaces with less network connectivity and shorter network lengths than LPI-KC and LPI-PC, which could explain its lower interfacial stiffness in response to shear and dilatational deformation. Combined with the lower $E_{\tau 1L}$ value of the LPI-SA stabilized interface, it most likely formed a weak gel or soft glass-like interface. In contrast, the LPI-KC stabilized interface formed by far the stiffest interface, consistent with its higher junction density, longer average vessel length, and lower lacunarity, and indicating that it may form a strong 2D gel-like interface. LPI had significantly lower contributions from odd harmonics than LPI-KC, but LPI and LPI-KC had comparable contributions from even harmonics. This result may indicate that LPI may form a more jammed glassy-like interface weaker in dilatational deformation, because of weaker in-plane interactions.

These strikingly different interfacial structures formed by LPI-KC, LPI-PC, and LPI-SA complexes could be attributed to their different morphological properties and flexibility. LPI-KC had a large, aggregated structure, consisting of several stiff chain molecules and globular protein clusters, forming a highly cross-linked structure, apparently cross-linked by individual proteins (~10 nm) and globular protein clusters (~100–150 nm). Upon adsorption at the interface, this structure may undergo structural rearrangement leading to cross-linking with other adsorbed complexes, and thus forming a densely packed interface with high network connectivity. Meanwhile, the structural rigidity of LPI-KC reduced the in-plane mobility of the interfacial network, resulting in a stiffer interface in response to shear and dilatational deformations. Regarding LPI-PC, its structure resembled a core-shell morphology with a dense core and pectin chains protruding from the core. As a result, LPI-PC formed a less densely packed interface than LPI-KC. LPI-SA adapted a smaller more linear morphology that lacked network cross-linking and interconnectivity in the structure. Moreover, the flexible chains inside LPI-SA complexes may have more structural mobility. This would explain the lower network stiffness ($E_{\tau 1L}$), the lower $U_{d\tau 2}$ and $U_{d\tau 3}$, and the lower vertical shift γ_s.

Additionally, LPI-KC could also develop a stiffer air-water interface than LPI-PC and LPI-SA at the initial adsorption phase (Fig. 3B and C). This phenomenon was most likely caused by both morphological characteristics and flexibility of complexes. The highly cross-linked structure of LPI-KC may enable the fast development of relatively tightly packed interfaces during the early adsorption period. The rigid molecular flexibility of LPI-KC further increased the resistance of the interface to the shear or dilatational deformations, resulting in the formation of a stiffer air-water interface. In contrast, LPI-PC and LPI-SA had less cross-linked

structures with more flexibility than LPI-KC, which may create loosely packed interfaces with lower network connectivity and more voids between globular molecules. As a result, these interfaces had more in-plane mobility and thus were less stiff in response to shear or dilatational deformation at the initial adsorption period.

3.6. Foaming properties of LPI-polysaccharide complexes

The foaming properties of LPI, LPI-KC, LPI-PC, and LPI-PC, including foamability and foam stability, were evaluated by whipping and gas sparging methods, respectively, according to our previous methods (Ma, Habibi, et al., 2024b). LPI at a concentration of 0.05 wt% showed largely higher foam overrun than LPI-PS complexes at 0.1 wt% of total concentration (0.05 wt% of protein concentration), while LPI at a concentration of 0.1 wt% showed comparable foam overrun with LPI-KC and LPI-PC at a total concentration of 0.2 wt% (0.1 wt% of protein concentration). Although LPI-KC and LPI-PC had significantly slower adsorption rates to the air-water interface than LPI due to their larger particle sizes, LPI-KC and LPI-PC could develop stiffer air-water interfaces in both shear and dilatational deformations in the early adsorption stages. These stiff interfaces at the early stage might offset the disadvantages caused by the slower adsorption rate, resulting in comparable foamability. In contrast, LPI-SA showed a significantly lower foam overrun than LPI, LPI-KC, and LPI-SA, especially at a total concentration of 0.2 wt%. LPI-SA showed a slower adsorption rate than LPI and also formed a markedly weaker interface in the initial adsorption stage than LPI-PC and LPI-KC, which overall resulted in the formation of a larger bubble size (Fig. 10C) and caused lower foamability.

At a total concentration of 0.1 wt%, LPI-KC and LPI-PC showed comparable foam stability to LPI at 0.05 wt%, but their stability was dramatically improved at a total concentration of 0.2 wt%, which was larger than LPI at 0.1 wt% (Fig. 10B). The higher interfacial stiffness of LPI-KC and LPI-PC than LPI could explain their more stable foam at a total concentration of 0.2 wt%. Additionally, LPI-KC showed a higher foam half-life time than LPI-PC at 0.2 wt% concentration, which was positively correlated to the interfacial properties, where LPI-KC formed stiffer air-water interface in response to shear and dilatational deformation than LPI-PC. LPI-SA-formed foams were extremely unstable regardless of concentration, although LPI-SA stabilized interfaces only showed slightly lower interfacial stiffness than LPI in dilatation. This observation might be caused by the adsorption kinetics. LPI-SA formed a weak interfacial layer in the initial adsorption period, which was unstable to bubble coalescence during foam formation and resulted in the formation of a large bubble size (Fig. 10C), that caused unstable foams for LPI-SA.

4. Conclusions

This study systematically investigated the influence of the morphological characteristics and flexibility of protein-polysaccharide complexes on the air-water interfacial and foaming properties. LPI-κ-carrageenan (KC) formed a large complex with a high degree of internal cross-linking, and hence high stiffness. LPI-pectin (PC) formed a core-shell morphology with a dense core and pectin chains protruding from that core. LPI-sodium alginate (SA) had a smaller more linear and flexible morphology with a lower degree of strand-strand cross-linking. Those morphological characteristics and flexibility were related to their interfacial and foaming properties. LPI-PC and LPI-SA diffused faster towards the air-water interfaces but formed markedly less stiff air-water interfaces in the early adsorption stage than LPI-KC. These two factors may offset to some extent, which resulted in a slightly higher foam overrun of LPI-PC than LPI-KC at 0.2 wt% of total concentration. Nevertheless, the weak interface of LPI-SA in the early adsorption stage caused the formation of large air bubbles, resulting in bubble coalescence and significantly lower foam overrun. After 3 h of adsorption, LPI-KC formed a strong 2D gel-like air-water interface with higher network connectivity, stiffer than the LPI-PC stabilized interfaces. As a result, the LPI-KC stabilized foams were more stable than the LPI-PC stabilized foams. In contrast, LPI-SA may form a weak gel or soft-glassy interface with a lower interfacial stiffness, which explains the unstable foam. In comparison with LPI at pH 4.0, LPI showed higher interfacial stiffness than LPI-SA but lower interfacial stiffness than LPI-KC and LPI-PC. As a result, LPI at 0.1 wt% formed a more stable foam than LPI-SA at 0.2 wt% of concentration, but less stable than LPI-KC and LPI-PC at 0.2 wt% of concentration.

Our findings from this study provide new insights into the air-water interfacial and foam stabilization mechanisms by lupin protein-polysaccharide complexes from the perspectives of their morphology and flexibility, an aspect that was not addressed in detail in previous studies on interfacial and foaming properties of protein-polysaccharide complexes (Guldiken et al., 2023; Han et al., 2024a, Han et al., 2024a; Liu, Xue, & Adhikari, 2023; X. Zhang et al., 2024). In these studies, only the foaming or emulsifying properties of protein-polysaccharide complexes made by different polysaccharide types are investigated and compared, without considering their morphologies and flexibilities. Our findings also provide possible explanations for similar results observed in other studies. For example, egg albumin-κ-carrageenan complexes formed foams that were more stable than egg albumin-guar gum complexes (Miquelim et al., 2010). This was most likely due to the different morphology of these complexes since κ-carrageenan is much more rigid than flexible guar gum, with an $L_p < 10$ nm (Picout et al., 2001), similar to SA. Understanding the role of morphological properties of complexes in interfacial and foam stabilization could help food manufacturers design complexes with tailored structures by choosing appropriate polysaccharides to achieve optimal foaming functionality.

CRediT authorship contribution statement

Xingfa Ma: Writing – original draft, Visualization, Validation, Methodology, Investigation, Formal analysis, Data curation,

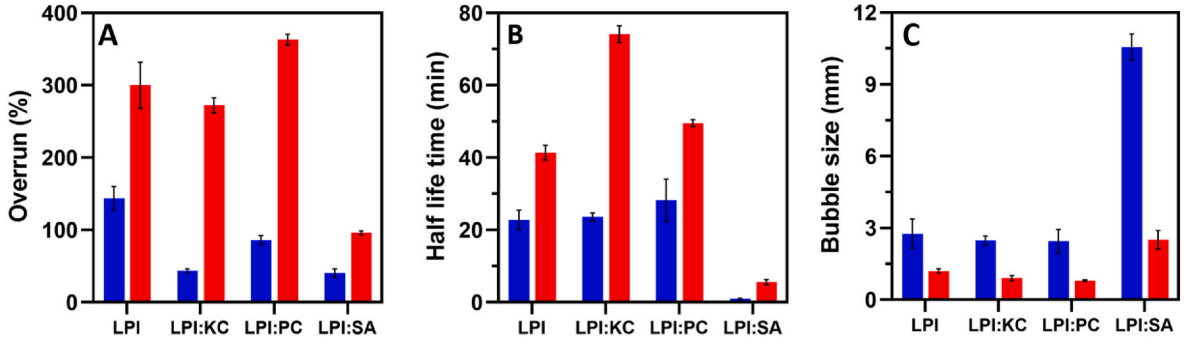

Fig. 10. Foam overrun (%) (A), half-life time (min) (B), and bubble size (mm) (C) of LPI-KC, LPI-PC, and LPI-SA at concentrations of 0.1 wt% ( ) and 0.2 wt% ( ). **NB**: the concentration of LPI in blue and red was 0.05 wt% and 0.1 wt%, respectively.

Conceptualization. **Mehdi Habibi:** Writing – review & editing, Supervision, Conceptualization. **Leonard M.C. Sagis:** Writing – review & editing, Supervision, Project administration, Funding acquisition, Conceptualization.

Declaration of competing interest

The authors have declared that no competing interest exists.

Acknowledgements

X. Ma acknowledges the funding from China Scholarship Council (CSC NO. 202207940007).

Appendix A. Supplementary data

Supplementary data to this article can be found online at https://doi.org/10.1016/j.foodhyd.2025.111247.

Data availability

Data will be made available on request.

References

Ahmad, S., Tanweer, M. S., Mir, T. A., Alam, M., Ikram, S., & Sheikh, J. N. (2023). Antimicrobial gum based hydrogels as adsorbents for the removal of organic and inorganic pollutants. *Journal of Water Process Engineering, 51*, Article 103377.

Akinchina, A., & Linse, P. (2002). Monte Carlo simulations of polyion– macroion complexes. 1. Equal absolute polyion and macroion charges. *Macromolecules, 35*(13), 5183–5193.

Alamanou, S., & Doxastakis, G. (1997). Effect of wet extraction methods on the emulsifying and foaming properties of lupin seed protein isolates (Lupinus albus ssp. Graecus). *Food Hydrocolloids, 11*(4), 409–413.

Aryee, F. N., & Nickerson, M. T. (2012). Formation of electrostatic complexes involving mixtures of lentil protein isolates and gum Arabic polysaccharides. *Food Research International, 48*(2), 520–527.

Aspinall, G. O. (2014). *The polysaccharides*. Academic press.

Banerjee, A., De, R., & Das, B. (2022). Hydrodynamic and conformational characterization of aqueous sodium alginate solutions with varying salinity. *Carbohydrate Polymers, 277*, Article 118855.

Bernklau, I., Lucas, L., Jekle, M., & Becker, T. (2016). Protein network analysis—a new approach for quantifying wheat dough microstructure. *Food Research International, 89*, 812–819.

Borgström, J., Egermayer, M., Sparrman, T., Quist, P.-O., & Piculell, L. (1998). Liquid crystallinity versus gelation of κ-carrageenan in mixed salts: Effects of molecular weight, salt composition, and ionic strength. *Langmuir, 14*(17), 4935–4944.

Boukid, F., & Pasqualone, A. (2022). Lupine (Lupinus spp.) proteins: Characteristics, safety and food applications. *European Food Research and Technology, 248*(2), 345–356.

Braudo, E., & Antonov, Y. (1993). Non-coulombic complex formation of protein as a structure forming factor in food systems. *Food Proteins, Structure and Functionality*, 210–215.

Buhler, E., & Boue, F. (2004). Chain persistence length and structure in hyaluronan solutions: Ionic strength dependence for a model semirigid polyelectrolyte. *Macromolecules, 37*(4), 1600–1610.

Burova, T. V., Grinberg, N. V., Grinberg, V. Y., Usov, A. I., Tolstoguzov, V. B., & de Kruif, C. G. (2007). Conformational changes in ι-and κ-carrageenans induced by complex formation with bovine β-casein. *Biomacromolecules, 8*(2), 368–375.

Campo, V. L., Kawano, D. F., da Silva Jr, D. B., & Carvalho, I. (2009). Carrageenans: Biological properties, chemical modifications and structural analysis–A review. *Carbohydrate Polymers, 77*(2), 167–180.

Ceresino, E. B., Johansson, E., Sato, H. H., Plivelic, T. S., Hall, S. A., Bez, J., et al. (2021). Lupin protein isolate structure diversity in frozen-cast foams: Effects of transglutaminases and edible fats. *Molecules, 26*(6), 1717.

de Groot, A., Yang, J., & Sagis, L. M. (2023). Surface stress decomposition in large amplitude oscillatory interfacial dilatation of complex interfaces. *Journal of Colloid and Interface Science, 638*, 569–581.

Doublier, J.-L., Garnier, C., Renard, D., & Sanchez, C. (2000). Protein–polysaccharide interactions. *Current Opinion in Colloid & Interface Science, 5*(3–4), 202–214.

Ghosh, A. K., & Bandyopadhyay, P. (2012). Polysaccharide-protein interactions and their relevance in food colloids. *Complex World Polysaccharides, 14*, 395–406.

Giménez-Ribes, G., Yang, J., He, Q., Habibi, M., & Sagis, L. M. (2023). Self-similarity and Payne effect of whey protein-escin mixtures at the air-water interface. *Food Hydrocolloids, 139*, Article 108554.

Girard, M., Turgeon, S. L., & Gauthier, S. F. (2003). Quantification of the interactions between β-lactoglobulin and pectin through capillary electrophoresis analysis. *Journal of Agricultural and Food Chemistry, 51*(20), 6043–6049.

Guemes-Vera, N., Martinez-Herrera, J., Hernandez-Chavez, J. F., Yanez-Fernandez, J., & Totosaus, A. (2012). Comparison of chemical composition and protein digestibility, carotenoids, tanins and alkaloids content of wild lupinus varieties flour. *Pakistan Journal of Nutrition, 11*(8), 676.

Guldiken, B., Saffon, M., Nickerson, M. T., & Ghosh, S. (2023). Improving physical stability of pea protein-based emulsions near the isoelectric point via polysaccharide complexation. *Food Hydrocolloids, 145*, Article 109029.

Han, Y., Zhu, L., Zhang, H., Liu, T., & Wu, G. (2024a). Characteristic of the interaction mechanism between soy protein isolate and functional polysaccharide with different charge characteristics and exploration of the foaming properties. *Food Hydrocolloids, 150*, Article 109615.

Han, Y., Zhu, L., Zhang, H., Liu, T., & Wu, G. (2024b). Understanding the foam stability mechanisms of complex formed by soy protein isolate and different charged polysaccharides: Air/water interfacial behavior and rheological characteristics. *International Journal of Biological Macromolecules, 268*, Article 131583.

Harding, S. E. (1997). The intrinsic viscosity of biological macromolecules. Progress in measurement, interpretation and application to structure in dilute solution. *Progress in Biophysics and Molecular Biology, 68*(2–3), 207–262.

Harding, S. E., Tombs, M. P., Adams, G. G., Paulsen, B. S., Inngjerdingen, K. T., & Barsett, H. (2017). *An introduction to polysaccharide biotechnology*. CRC Press.

Huang, L., Yan, Y., Qu, L., Li, F., Chen, L., & Li, Y. (2024). Structure, emulsifying and embedding characteristics of soy protein isolate induced by the complexation of carrageenan with different charge groups. *Food Hydrocolloids*, Article 110455.

Hyun, K., Kim, S. H., Ahn, K. H., & Lee, S. J. (2002). Large amplitude oscillatory shear as a way to classify the complex fluids. *Journal of Non-newtonian Fluid Mechanics, 107*(1–3), 51–65.

Jaishankar, A., & McKinley, G. H. (2013). Power-law rheology in the bulk and at the interface: Quasi-properties and fractional constitutive equations. *Proceedings of the Royal Society A: Mathematical, Physical and Engineering Sciences, 469*(2149), Article 20120284.

Klassen, D., & Nickerson, M. (2012). Effect of pH on the formation of electrostatic complexes within admixtures of partially purified pea proteins (legumin and vicilin) and gum Arabic polysaccharides. *Food Research International, 46*(1), 167–176.

Koren, R., & Hammes, G. G. (1976). A kinetic study of protein-protein interactions. *Biochemistry, 15*(5), 1165–1171.

Ledward, D. A. (1994). Protein–polysaccharide interactions. *Protein functionality in food systems*.

Liu, X., Xue, F., & Adhikari, B. (2023). Hemp protein isolate-polysaccharide complex coacervates and their application as emulsifiers in oil-in-water emulsions. *Food Hydrocolloids, 137*, Article 108352.

Lo, B., Kasapis, S., & Farahnaky, A. (2020). Lupin protein: Isolation and techno-functional properties, a review. *Food Hydrocolloids, 112*(March 2021).

Lucassen, J., & Van Den Tempel, M. (1972). Dynamic measurements of dilational properties of a liquid interface. *Chemical Engineering Science, 27*(6), 1283–1291.

Ma, X., Habibi, M., & Sagis, L. M. (2024a). Interfacial and foaming properties of soluble lupin protein isolates: Effect of pH. *Food Hydrocolloids*, Article 110228.

Ma, X., Habibi, M., & Sagis, L. M. (2024b). pH-induced conformational changes of lupin protein-pectin mixtures and its effect on air-water interfacial properties and foaming functionality. *Food Hydrocolloids*, Article 110567.

Ma, X., Shen, P., Habibi, M., & Sagis, L. M. (2024). Interfacial properties and functionality of lupin protein-pectin complexes at the air-water interface. *Food Hydrocolloids*, Article 110050.

McClements, D. J. (2006). Non-covalent interactions between proteins and polysaccharides. *Biotechnology Advances, 24*(6), 621–625.

Mekhloufi, G., Sanchez, C., Renard, D., Guillemin, S., & Hardy, J. (2005). pH-induced structural transitions during complexation and coacervation of β-lactoglobulin and acacia gum. *Langmuir, 21*(1), 386–394.

Melo, T. S., Ferreira, R. B., & Teixeira, A. N. (1994). The seed storage proteins from Lupinus albus. *Phytochemistry, 37*(3), 641–648.

Miquelim, J. N., Lannes, S. C., & Mezzenga, R. (2010). pH Influence on the stability of foams with protein–polysaccharide complexes at their interfaces. *Food Hydrocolloids, 24*(4), 398–405.

Mohnen, D. (2008). Pectin structure and biosynthesis. *Current Opinion in Plant Biology, 11*(3), 266–277.

Morris, G. A., de al Torre, J. G., Ortega, A., Castile, J., Smith, A., & Harding, S. E. (2008). Molecular flexibility of citrus pectins by combined sedimentation and viscosity analysis. *Food Hydrocolloids, 22*(8), 1435–1442.

Morris, G., Foster, T., & Harding, S. (2000). The effect of the degree of esterification on the hydrodynamic properties of citrus pectin. *Food Hydrocolloids, 14*(3), 227–235.

Munialo, C. D., van der Linden, E., Ako, K., & de Jongh, H. H. (2015). Quantitative analysis of the network structure that underlines the transitioning in mechanical responses of pea protein gels. *Food Hydrocolloids, 49*, 104–117.

Muranyi, I. S., Otto, C., Pickardt, C., Osen, R., Koehler, P., & Schweiggert-Weisz, U. (2016). Influence of the isolation method on the technofunctional properties of protein isolates from Lupinus angustifolius L. *Journal of Food Science, 81*(11), C2656–C2663.

Picout, D. R., Ross-Murphy, S. B., Errington, N., & Harding, S. E. (2001). Pressure cell assisted solution characterization of polysaccharides. 1. Guar gum. *Biomacromolecules, 2*(4), 1301–1309.

Qiu, W.-Y., Cai, W.-D., Wang, M., & Yan, J.-K. (2019). Effect of ultrasonic intensity on the conformational changes in citrus pectin under ultrasonic processing. *Food Chemistry, 297*, Article 125021.

Rodés-Bachs, C., & Van der Fels-Klerx, H. (2023). Impact of environmental factors on the presence of quinolizidine alkaloids in lupins: A review. *Food Additives & Contaminants: Part A, 40*(6), 757–769.

Sanchez, C., Despond, S., Schmitt, C., & Hardy, J. (2001). *Effect of heat and shear on β-lactolobulin-acacia gum complex coacervation*.
Schmidt, I., Novales, B., Boué, F., & Axelos, M. A. (2010). Foaming properties of protein/pectin electrostatic complexes and foam structure at nanoscale. *Journal of Colloid and Interface Science, 345*(2), 316–324.
Schmitt, C., Sanchez, C., Desobry-Banon, S., & Hardy, J. (1998). Structure and technofunctional properties of protein-polysaccharide complexes: A review. *Critical Reviews in Food Science and Nutrition, 38*(8), 689–753.
Schmitt, C., & Turgeon, S. L. (2011). Protein/polysaccharide complexes and coacervates in food systems. *Advances in Colloid and Interface Science, 167*(1–2), 63–70.
Shrestha, S., van't Hag, L., Haritos, V. S., & Dhital, S. (2021). Lupin proteins: Structure, isolation and application. *Trends in Food Science & Technology, 116*, 928–939.
Stoll, S., & Chodanowski, P. (2002). Polyelectrolyte adsorption on an oppositely charged spherical particle. Chain rigidity effects. *Macromolecules, 35*(25), 9556–9562.
Tanoeiro, J. R., Fortunato, D., Cotas, J., Morais, T., Afonso, C., & Pereira, L. (2023). Different Chondrus crispus aquaculture methods and carrageenan extraction. *Applied Sciences, 13*(9), 5466.
Turgeon, S., Beaulieu, M., Schmitt, C., & Sanchez, C. (2003). Protein–polysaccharide interactions: Phase-ordering kinetics, thermodynamic and structural aspects. *Current Opinion in Colloid & Interface Science, 8*(4–5), 401–414.
Turgeon, S., Schmitt, C., & Sanchez, C. (2007). Protein–polysaccharide complexes and coacervates. *Current Opinion in Colloid & Interface Science, 12*(4–5), 166–178.
Wan, Y., Lin, C., Li, Y., Wang, R., Feng, W., Chen, Z., et al. (2023). Tuning the electrostatic interaction between rice protein and carboxymethyl cellulose toward hydrophilic composites with enhanced functional properties. *International Journal of Biological Macromolecules, 235*, Article 123918.
Wang, J., & Nie, S. (2019). Application of atomic force microscopy in microscopic analysis of polysaccharide. *Trends in Food Science & Technology, 87*, 35–46.
White, C. L., & Staines, V. E. (2007). A review of the nutritional value of lupins for dairy cows. *Australian Journal of Agricultural Research, 58*(3), 185–202.
Wierenga, P. A., Meinders, M. B., Egmond, M. R., Voragen, F. A., & de Jongh, H. H. (2003). Protein exposed hydrophobicity reduces the kinetic barrier for adsorption of ovalbumin to the air− water interface. *Langmuir, 19*(21), 8964–8970.
Winter, H. H., & Mours, M. (1999). Rheology of polymers near liquid-solid transitions. *Neutron spin echo spectroscopy viscoelasticity rheology* (pp. 165–234).
Xu, Y., Yang, N., Yang, J., Hu, J., Zhang, K., Nishinari, K., et al. (2020). Protein/polysaccharide intramolecular electrostatic complex as superior food-grade foaming agent. *Food Hydrocolloids, 101*, Article 105474.
Zhang, J., Du, H., Ma, N., Zhong, L., Ma, G., Pei, F., et al. (2023). Effect of ionic strength and mixing ratio on complex coacervation of soy protein isolate/Flammulina velutipes polysaccharide. *Food Science and Human Wellness, 12*(1), 183–191.
Zhang, J., & Liu, X. Y. (2003). Effect of protein–protein interactions on protein aggregation kinetics. *The Journal of Chemical Physics, 119*(20), 10972–10976.
Zhang, X., Wang, Y., Li, Z., Li, Y., & Qi, B. (2024). Effects of polysaccharide type on the structure, interface behavior, and foam properties of soybean protein isolate hydrolysate-polysaccharide Maillard conjugates. *Food Hydrocolloids, 151*, Article 109801.